Modeling-based design and assessment of an acousto-optic guided high-intensity focused ultrasound system

Matthew T. Adams
Robin O. Cleveland
Ronald A. Roy

SPIE.

Modeling-based design and assessment of an acousto-optic guided high-intensity focused ultrasound system

Matthew T. Adams,[a,b,][*] **Robin O. Cleveland,**[b] **and Ronald A. Roy**[c]
[a]Boston University, Department of Mechanical Engineering, 110 Cummington Mall, Boston, Massachusetts 02215, United States
[b]University of Oxford, Institute of Biomedical Engineering, Department of Engineering Science, Old Road Campus Research Building, Oxford OX3 7DQ, United Kingdom
[c]University of Oxford, Department of Engineering Science, 9 Parks Road, Oxford OX1 3PJ, United Kingdom

Abstract. Real-time acousto-optic (AO) sensing has been shown to noninvasively detect changes in *ex vivo* tissue optical properties during high-intensity focused ultrasound (HIFU) exposures. The technique is particularly appropriate for monitoring noncavitating lesions that offer minimal acoustic contrast. A numerical model is presented for an AO-guided HIFU system with an illumination wavelength of 1064 nm and an acoustic frequency of 1.1 MHz. To confirm the model's accuracy, it is compared to previously published experimental data gathered during AO-guided HIFU in chicken breast. The model is used to determine an optimal design for an AO-guided HIFU system, to assess its robustness, and to predict its efficacy for the ablation of large volumes. It was found that a through transmission geometry results in the best performance, and an optical wavelength around 800 nm was optimal as it provided sufficient contrast with low absorption. Finally, it was shown that the strategy employed while treating large volumes with AO guidance has a major impact on the resulting necrotic volume and symmetry. © *2017 Society of Photo-Optical Instrumentation Engineers (SPIE)* [DOI: [10.1117/1.JBO.22.1.017001](#)]

Keywords: high-intensity focused ultrasound; guidance; acousto-optic; Monte Carlo; modeling; thermal damage.

Paper 160667R received Sep. 27, 2016; accepted for publication Dec. 27, 2016; published online Jan. 23, 2017.

1 Introduction

High-intensity focused ultrasound (HIFU)—a noninvasive surgical technique in which highly localized heating caused by the absorption of focused ultrasound results in irreversible tissue necrosis—is an emerging treatment modality for solid tumors,[1,2] uterine fibroids,[3] essential tremor,[4] and other conditions.[5] As HIFU is completely noninvasive and treatment planning is difficult due to patient and time-dependent environmental factors, a reliable treatment monitoring and guidance technique is imperative for its efficacy and its clinical acceptance.[6] To date, diagnostic ultrasound[7–9] and magnetic resonance (MR) imaging thermometry[1,10] are the only two guidance methods that have seen clinical use.

Although diagnostic ultrasound scanners are inexpensive, portable, and capable of imaging in real time, there is insufficient contrast between necrotic and healthy tissue to reliably image HIFU lesions unless the exposure generates boiling within the tissue,[11–15] resulting in unpredictable and abnormally formed lesions.[16–18] Moreover, it is possible to generate HIFU lesions in tissue without boiling or excessive cavitation activity, resulting in necrotic tissue that is not readily visible on a diagnostic ultrasound scan. MR thermometry, on the other hand, is able to provide quasi-real time temperature measurements *in situ* with spatial resolution on the order of 1 mm and temporal resolution on the order of 1 frame/s.[6] Temperature measurements are then used to calculate the thermal dose[19] delivered to the tissue from which one can infer thermal damage. MR thermometry

is currently considered the "gold standard" for HIFU guidance.[6,20] However, MR guided HIFU systems are expensive, complex, nonportable, and sensitive to patient movement,[2] eliciting the motive for new approaches to monitoring lesion formation, preferably in real time.

In contrast to the two clinical HIFU monitoring methods, which sense indirect indicators of thermal damage, there are several experimental methods under investigation that directly image or sense tissue properties that change with thermal damage, such as elasticity,[21,22] photoacoustic properties,[23] or optical properties.[24,25] In the latter case, both the optical scattering, μ_s, and absorption, μ_a, coefficients of the tissue increase due to the thermal dissociation of phospholipid cellular membranes and thermal denaturation of intracellular and extracellular proteins.[26] Additionally, the formation of methemoglobin from hemoglobin during blood coagulation has been shown to cause a further increase in the absorption coefficients of tissues.[27] Recently, real-time acousto-optic (AO) sensing of thermally induced changes in the optical properties of *ex vivo* tissues has been demonstrated during noncavitating HIFU exposures.[24,25] When tissue is illuminated by diffuse light and insonified with HIFU, the light that passes through the HIFU focus becomes phase modulated by periodic density variations and periodic displacements of scattering sites.[28–31] By monitoring changes in the flux of phase-modulated light, one can directly monitor changes in optical scattering and absorption caused by HIFU-induced heating in the focus. The same sound field is used both to induce heating and pump the AO phase modulations; thus, the sensing and treatment volumes are automatically co-registered.

*Address all correspondence to: Matthew T. Adams, E-mail: [adamsm2@bu](#) [.edu](#)

Although this technique has been demonstrated *ex vivo*, it has not been optimized to work in a clinical setting and the parameters affecting the AO detectability of HIFU lesions are not well understood. The goal of this study is to use a modeling-based approach to determine the optimal design for an AO-guided HIFU system, to develop a treatment strategy for the ablation of large volumes, and to assess the robustness of the system's signal to changes in tissue thickness, lesion properties, and lesion location. In the following section, the full model and its implementation are presented along with the relevant acoustic, thermal, optical, and AO theory. Next, we demonstrate the effect of system design parameters on lesion detectability and we test the robustness of the system to changes in environmental variables by varying tissue thickness, lesion location, and optical contrast. In this section, we also present a comparison between the model and previously published experimental data. Finally, a strategy for ablating large volumes with AO guidance is described.

2 Modeling Methodology

The model developed here seeks to simulate the entire AO-guided HIFU process. To do so, the acoustic field from the HIFU source and the diffusive optical field inside the tissue must be calculated. The acoustic field is used to determine the temperature rise and subsequent changes in tissue properties, and to calculate the phase modulations imparted on the optical field. Finally, the phase modulated light is used to calculate a detected AO signal. Each of these processes is described here.

2.1 Ultrasound Propagation

The three-dimensional pressure, particle velocity, and intensity distributions from a single element, spherically focused HIFU source (based on model H-102, Sonic Concepts, WA) with a 70-mm aperture, a 20-mm diameter central hole, and a 62.4-mm focal length operating at 1.1 MHz were calculated using the angular spectrum method,[32,33] which allows the prediction of linear diffractive fields. The source condition of the focused source on a flat plane was accomplished using the method of Ref. [34]. The hole in the center of the H-102 transducer was accounted for by employing Babinet's principle and subtracting the solution for a transducer of the same size and curvature as the hole.[35] For all of the simulations performed in this work, a grid spacing of 100 μm was used, the source was directed along the $+z$ axis, and the calculation domain was extended to five times the radius of the source in x and y. The calculation domain was large in order to minimize the effect of mirror sources in the solution. The 100-μm grid spacing is smaller than what is required to obtain an accurate solution, but it was chosen to be compatible with the fine grid spacing required for the AO Monte Carlo (MC) simulations. The angular spectrum solution was validated by comparison to an analytical solution to the on-axis and focal-plane pressure of a focused radiator,[36] and the root mean-squared errors were found to be well under 1% of the maximum pressure at a grid spacing of 100 μm.

In order to calculate acoustic propagation from water into tissue, both media were treated as semi-infinite layers. The angular spectrum solution was calculated at each step along the acoustic propagation axis until it reached the tissue boundary, where a transmission coefficient was calculated. Changes in propagation direction due to refraction at the tissue boundary were assumed to be negligible, and an angularly dependent transmission coefficient was not considered, resulting in an error of <1% in the worst-case scenario. Figure 1 shows the calculated
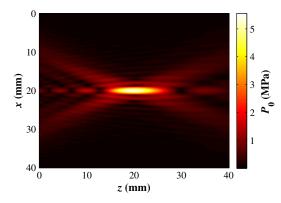

Fig. 1 Calculated pressure magnitude, P_0, along the axial plane ($y = 20$ mm) inside chicken breast insonified at 1.1 MHz by an H-102 HIFU source. The source was positioned at $(x,y,z) = 20, 20, -32$ and directed along the $+z$-axis with a peak focal pressure amplitude of 5.6 MPa. The sound propagated through water before entering the chicken breast at $z = 0$. The acoustic properties of the medium are defined in Table 1 and a grid spacing of 100 μm was used.

pressure magnitude, P_0, along the axial plane inside a cube of chicken breast submerged in water. The 1.1-MHz HIFU source is positioned at $(x, y, z) = (20, 20, -32)$ mm, and the sound propagated through water in $+z$ until it reached $z = 0$, where it was transmitted into the chicken breast. We selected an ultrasound source pressure that yielded a spatial peak focal pressure of 6 MPa in water. The corresponding focal pressure in the tissue was 5.6 MPa, owing to a greater level of ultrasound attenuation in chicken breast. The acoustic properties used to generate Fig. 1 are given in Table 1.

The distribution of the time-averaged intensity, I_{av}, inside the chicken breast was calculated as follows:

$$I_{av} = \Re\left(\frac{1}{2}P^*V\right), \qquad (1)$$

where P^* is the complex conjugate of the pressure field, and the complex particle velocity field, V, is calculated as follows:

$$V = \frac{-\nabla P}{i\rho_0\omega_a}, \qquad (2)$$

where ρ_0 is density and ω_a is the acoustic angular frequency. The directional vector of the particle velocity field, $\hat{V}(x, y, z, t)$, is also used for calculating AO phase modulations.

Table 1 The acoustic properties of water and chicken breast used in the angular spectrum simulation. ρ_0 is density, c_a is the speed of sound, and α is the total attenuation coefficient. The acoustic absorption coefficient, α_a, is the fraction of the total attenuation that contributes to heating in the tissue. Distortion in the pressure field due to acoustic scattering is relatively small in both water and tissue and is not considered in this work.

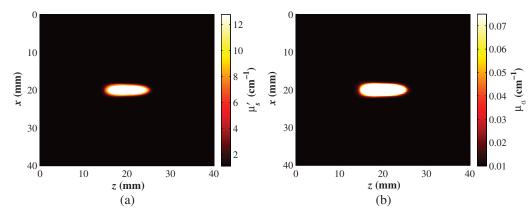| Property	Water	Chicken breast
c_a (m/s)	1481	1585
ρ_0 (kg/m³)	998	1040
α (Np/m)	0.025	0.555
α_a (Np/m)	0.025	0.433

Fig. 2 (a) Calculated reduced scattering, μ_s' and (b) absorption, μ_a coefficients at 1064 nm along the axial plane ($y = 20$ mm) inside chicken breast after a 60-s HIFU exposure with a peak focal pressure amplitude of 5.6 MPa. The source was positioned at $(x, y, z) = (20, 20, -32)$ mm and directed along the $+z$-axis. The acoustic, thermal, and optical properties used to generate the figure are defined in Tables 1, 2, and 3, respectively. A grid spacing of 100 μm and a time step of 100 ms were used in the simulations.

2.2 Tissue Heating and Optical Property Changes

Temperature increases due to the absorption of ultrasound were modeled using the Pennes bioheat transfer equation:[37]

$$\rho_0 C_v \frac{\partial T}{\partial t} = K\nabla^2 T - W_b C_b (T - T_a) + q_m + 2\alpha_a |I_{av}|, \qquad (3)$$

where C_v is specific heat capacity, T is tissue temperature, t is time, K is thermal conductivity, W_b is the blood perfusion coefficient of the tissue, C_b is the heat capacity of blood, T_a is the ambient blood temperature, q_m is the power density of metabolic heat generation, and α_a is the acoustic absorption coefficient. For all of the simulations presented here, blood perfusion and metabolic heat generation, and thus, the second and third terms on the right-hand-side of Eq. (3), were neglected. Equation (3) was solved using an alternating direction modification to the Crank–Nicolson finite-difference approach.[38] The temperature solution was validated by comparison to an analytical solution to the focal temperature change induced by a heat source extending infinitely along an axis with a Gaussian radial profile.[39,40] Given a 100-μm grid spacing and a 100-ms time step, a maximum error of ~1.5% was calculated for all heating times and rates investigated.

Given the temperature increase during a time step Δt, the thermal dose accumulated in that time, Δt_{43}, is calculated as follows:[19]

$$\Delta t_{43} = R^{43 - T_{avg}} \Delta t, \qquad (4)$$

where Δt is expressed in minutes and T_{avg} is the average temperature in the voxel during Δt. The isodose constant, R, was taken as 0.25 for $T_{avg} < 43$°C and 0.63 for $T_{avg} > 43$°C based on measurements we have reported for changes in the optical properties of chicken breast.[41] Given the total accumulated thermal dose, t_{43} in a voxel after each time step, the optical reduced scattering, μ_s', and absorption, μ_a, coefficients are calculated as follows:

$$\mu = \mu_0 + (\Delta\mu)_{max} \left[1 - \exp\left(-\frac{t_{43}}{\tau_{43}}\right) \right], \qquad (5)$$

where μ_0 is the initial value of the coefficient, $(\Delta\mu)_{max}$ is the maximum observable change in the coefficient, and τ_{43} is the

thermal dose constant that governs the rate at which the property changes.[41] Changes in acoustic properties were not considered here.

Figure 2 shows μ_s' and μ_a at 1064 nm along the axial plane ($y = 20$ mm) inside a $40 \times 40 \times 40$ mm^3 chicken breast after a 60-s HIFU exposure with a peak focal pressure amplitude of 5.6 MPa, resulting in an ~30-mm^3 lesion. The thermal[42] and optical[41] properties used to generate Fig. 2 are given in Tables 2 and 3 respectively.

2.3 Light Propagation and Acousto-Optic Interactions

The gold standard for modeling light propagation in turbid media, such as tissue, is the MC method.[43] In our study, an open-source graphics processing unit (GPU) accelerated MC light propagation algorithm[44] was modified to account for light–sound interactions and AO signal detection. Calculations of ultrasound-induced phase modulations were implemented in a procedure similar to that of Ref. 45 and are briefly summarized here.

For each photon packet step of length l_i within a given voxel, the phase increment accumulated by the packet due to the modulation of the refractive index, $\Delta\phi_{n,i}$, was calculated as follows:

$$\Delta\phi_{n,i} = \frac{k_0 n_0 l_i \eta}{\rho_0 c_a^2} P(t), \qquad (6)$$

where n_0 is the refractive index of the tissue, η is the elasto-optic coefficient of the tissue, c_a is the speed of sound in the tissue,

Table 2 The thermal properties of chicken breast used in all of the bioheat transfer simulations.[42] C_v is the specific heat, K is the thermal conductivity, and W_b is the blood perfusion coefficient.

Property	Value
C_t (J/kg · C)	3210
K_t (W/m · C)	0.4683
W_b (kg/m^3 · s)	0

Table 3 The optical properties of chicken breast at 1064 nm used in all simulations.[41]

Property	Value
$\mu_{a,0}$ (cm^{-1})	0.01
$(\Delta\mu_a)_{max}$ (cm^{-1})	0.065
$\tau_{43}(\mu_a)$ (min)	598
$\mu'_{s,0}$ (cm^{-1})	1.1
$(\Delta\mu'_s)_{max}$ (cm^{-1})	7.535 if T_{max} < 70°C
	11.66 if T_{max} > 70°C
$\tau_{43}(\mu'_s)$ (min)	2214
n_0	1.4
g	0.9
η	0.32

$k_0 = 2\pi/\lambda_0$ is the optical wavenumber in vacuo, and $P(t)$ is the pressure calculated by the angular spectrum solution. Similarly, for each scattering event j, the phase increment accumulated by the packet due to the ultrasound-induced scatterer displacement, $\Delta\phi_{d,j}$, was calculated as follows:

$$\Delta\phi_{d,j} = k_0 n_0 (\hat{\Omega}_{inc} - \hat{\Omega}_{sc}) \cdot \vec{\xi}(t), \tag{7}$$

where $\hat{\Omega}_{inc}$ is the direction of the incident photon packet, $\hat{\Omega}_{sc}$ is the direction of the scattered photon packet, and $\vec{\xi}(t)$ is the displacement of the scatterer, which is assumed to follow the background medium in amplitude, phase, and direction.

At each step, the total ultrasound-induced phase shift, ϕ_s, of the photon packet was calculated as follows:

$$\phi_s = \sum_i \Delta\phi_{n,i} + \sum_j \Delta\phi_{d,j}, \tag{8}$$

and the power spectrum of the packet was calculated from ϕ_s and its packet weight, W_s. (A photon packet is a physical abstraction of a group of photons traveling in a common direction with a total energy given by their packet weight, W_s.) At each scattering event, a portion of the packet weight, $J_0^2(|\phi_s|)W_s$, was added to the voxel's unmodulated fluence, Φ_0, and a portion $2J_1^2(|\phi_s|)W_s$ was added to the voxel's modulated fluence, Φ_1,[45] where J_n is a Bessel function of the n'th order.

In order to model the detection of AO signals, circular detectors were placed at the tissue boundaries. If a photon packet reached a detector, its weight, W_s, and its total phase shift were recorded. At the completion of the simulation, the total radiant flux, F_t, to reach each detector was calculated as follows:

$$F_t = S_0 \sum_s W_s, \tag{9}$$

where S_0 is the illumination source power and W_s is summed over all detected photon packets. The detected AO signal, F_{AO}, is modeled as a photorefractive crystal (PRC) based detector.[46] At each detector, F_{AO} is given as follows:

$$F_{AO} = 2\eta_{det} S_0 e^{-\alpha_c L_c} [e^{\gamma' L_c} \cos(\gamma'' L_c) - 1] \sum_s W_s [J_0(|\phi_s|) - 1], \tag{10}$$

where η_{det} is the efficiency of the light collection optics, α_c is the optical absorption coefficient of the crystal, L_c is the optical path length of the crystal, and $\gamma = \gamma' + i\gamma''$ is the two-wave mixing gain coefficient of the crystal. Although AO signals were modeled to simulate PRC detection, they are directly proportional to the modulated fluence Φ_1. Therefore, the results presented in this work are applicable to any detection paradigm that is proportional to Φ_1.

In order to conform with the small phase approximations used in developing this model,[30] the acoustic field from the angular spectrum solution is normalized to a peak pressure of 100 kPa for the AO simulations. Because 100 kPa is far lower than the pressure amplitudes typically used during HIFU, calculations of phase modulations and F_{AO} are significantly lower than what should be expected during HIFU. However, for the studies presented in this work, we are interested in the AO signal contrast, ΔAO [defined by Eq. (11)], and not the magnitude of F_{AO}. Preliminary simulations (data not shown) indicated that ΔAO is independent of pressure amplitude.

The light propagation component of the MC algorithm has previously been validated by comparisons to the diffusion equation,[44] and the validation studies were repeated for this work. The AO component of the algorithm was validated by comparison to an analytical solution for a slab geometry with a cylindrical inclusion of plane-wave ultrasound presented by Ref. 47. This is the same method of validation used by Ref. 48, and a similar level of agreement to the analytical solution was achieved.

Figures 3(a) and 3(c) show the distribution of Φ_0 and Figs. 3(b) and 3(d) show the distribution of Φ_1 inside of an optically homogeneous $40 \times 40 \times 40$ mm^3 [Figs. 3(a) and 3(b)] and lesioned [Figs. 3(c) and 3(d)] chicken breast (see Fig. 2 for optical properties) insonified at 1.1 MHz with a peak focal pressure amplitude of 100 kPa and illuminated with a 1064-nm pencil beam source at $(x, y, z) = (0, 20, 20)$ mm directed along the $+x$-axis. The lesioned medium shown in (c) and (d) is the volume shown in Fig. 2. One billion photon packets were simulated for each condition. The acoustic and optical properties used to generate Fig. 3 are described in Tables 1 and 3, respectively.

3 Results

3.1 Overview

Unless otherwise stated, the simulation medium for all the results presented in this study was a $40 \times 40 \times 40$ mm^3 cube of chicken breast with a grid spacing of 100 μm immersed in water. The acoustic properties of the chicken and the water are given in Table 1, and the thermal and optical properties of the chicken are given in Tables 2 and 3, respectively. A time step of 100 ms was used for all thermal calculations. In every case, the tissue was insonified along the $+z$-axis and the pressure field co-registered with the lesion. Unless otherwise stated, the tissue was illuminated with a 1064-nm pencil beam positioned at the center of the $x = 0$ plane and launching 100 million photons directed in $+x$ [as shown by S$_2$ in Fig. 4(a)], and a 20-mm radius detection aperture was placed in the center of the tissue boundary at the maximum x dimension [D$_4$ in Fig. 4(a)]. The detector properties used for each simulation are listed in Table 4.
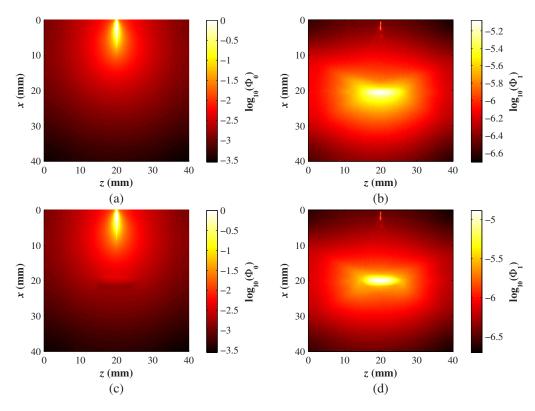
Fig. 3 (b, d) Log_{10} of the modulated and (a, c) unmodulated fluence inside of an (a, b) optically homogeneous and (c, d) lesioned $40 \times 40 \times 40$ mm chicken breast insonified at 1.1 MHz with a peak pressure of 100 kPa and illuminated with a 1064-nm pencil beam source at $(x, y, z) = (0, 20, 20)$ mm directed along the $+x$-axis. The lesioned volume is that shown in Fig. 2. The acoustic and optical properties used to generate the figure are defined in Tables 1 and 2, respectively. A grid spacing of 100 μm and 1 billion photons were used in the simulations. Note that the scale of each figure is different, and the numbers on the colorbars are in logarithmic format.

For thermal simulations, the peak focal pressure amplitude was scaled up to 5.6 MPa so that a lesion the same size as the HIFU focal region could be formed in 60 s. This likely violates the linear approximation used to calculate the acoustic field, but considering nonlinear effects was beyond the scope of this work. This exposure resulted in a lesion of approximately the same size as the HIFU focus ($\sim$30 mm^3) in the center of the volume, as shown in Fig. 2. For each of the simulations presented here, the AO "signal contrast" of a lesion is evaluated. We define the AO signal contrast, ΔAO, of a lesion as follows:

$$\Delta \mathrm{AO} = \frac{|F_{\mathrm{AO},l} - F_{\mathrm{AO},0}|}{F_{\mathrm{AO},0}} \times 100\%, \qquad (11)$$

where $F_{\mathrm{AO},l}$ is the detected AO signal in the presence of a lesion and $F_{\mathrm{AO},0}$ is the detected AO signal in the absence of a lesion.

3.2 System Design

Three aspects of the AO system for HIFU lesion detection will be considered: (i) illumination/detection geometry, (ii) detection aperture size, and (iii) optical wavelength. The goal is to find a geometry that maximizes the signal contrast of a lesion while maintaining a reasonable SNR so that guidance can be performed in real time. For organs with good acoustic and optical accessibility, such as breast, many different geometries can be considered. However, other organs—such as liver, kidney, and

bone—offer limited optical access, e.g., only one or two sides of the organ. In this section, we attempt to illustrate the optimal illumination/detection geometry for organs with good optical access, while also demonstrating the effect of having access to only one or two sides of an organ. The effect of the detection aperture size is also investigated. The optical wavelength is an important parameter, as it dictates how the light interacts with the tissue and the ultrasound, and it also affects the contrast in the optical properties between lesioned and unlesioned tissue.

In order to examine the effect of the illumination/detection geometry on AO signal contrast, a 5-mm diameter spherical inclusion with the optical properties of a HIFU lesion was placed in the center of the otherwise homogeneous volume. A spherical inclusion was used here in place of the HIFU lesion to avoid effects caused by the lesion's asymmetry. As shown in Fig. 4(a), optical sources at 0 deg (S_1), 90 deg (S_2), and 180 deg (S_3) relative to the HIFU propagation were considered.

For each of these sources, the AO signal contrast was evaluated for transmission, reflection, and side detection, in which case the detector needed to be in one of five positions, D_1 through D_5. These nine different geometries are described in Fig. 4(a) and Table 5.

Figure 4(b) shows the AO contrast for each of the nine configurations. It can be seen that the highest contrast is for a source at 90 deg to the HIFU and the optical detector in through transmission (S_2/D_4). This yields nearly a three times better contrast than any other illumination/detection geometry. However, this strategy is possible only for an organ with good optical access.
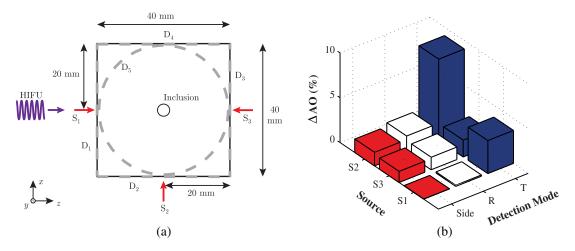
Fig. 4 (a) A cross-section from the center of the volume showing the 5-mm diameter spherical inclusion. The locations of the five 20-mm radius circular detection apertures are shown with dashed gray lines and the locations of the three optical sources are shown with red arrows. D_1 through D_4 appear as straight lines on the sides of the tissue because they are seen from a top view. D_5's circular aperture can be seen on the top of the tissue in the xz plane. (b) AO signal contrast of the spherical inclusion for the nine illumination/detection geometries described in Table 5. The bulk medium had the optical properties of chicken breast at 1064 nm, while the inclusion had optical properties of a lesion at 1064 nm, as defined in Table 3. The acoustic properties used to generate the figure are defined in Table 1.

For investigating the size of the detection aperture, the optimal illumination/detection geometry (illuminating with S_2 and detecting with D_4) was employed and the detector was modeled as a disc of varying radius. Figure 5(a) shows the AO signal contrast and Fig. 5(b) shows the normalized AO signal magnitude of the $\sim$30 mm^3 HIFU lesion shown in Fig. 2 as a function of the detection aperture radius. It can be seen that using a smaller aperture results in a slightly better contrast—as it minimizes the collection of light that has accumulated phase-shifts outside of the HIFU focus—but it comes at the expense of the signal's magnitude, and thus its SNR. The magnitude of the AO signal is proportional to the radiant flux of the light collected by the aperture; therefore, it is expected that it would decay exponentially with the size of the detection aperture.

The final design consideration is the impact of the optical wavelength on the AO signal. In standard diffuse optical imaging (without AO interactions), it is normally preferable to illuminate at an optical wavelength, where the transport coefficient, $\mu_t' = \mu_s' + \mu_a$, is lowest (provided the optical contrast is sufficient at this wavelength). When μ_t' is minimized, the penetration depth of the light will be maximized. For an AO system, it is not

as obvious that this is the best strategy because the wavelength of the light will also impact the AO phase modulations.

Table 6 shows the AO signal magnitude (normalized by the illumination fluence) and the signal contrast of the $\sim$30 mm^3 HIFU lesion for a variety of optical wavelengths. These wavelengths were chosen for either their biological relevance (minima or maxima in chromophore absorption spectra) or technical relevance (common laser wavelength). The highest AO contrast occurs at 500 nm, but this wavelength results in the lowest detected radiant flux. The highest radiant flux is observed at 660 nm, but the AO contrast is second lowest at this point. Optimizing the wavelength therefore depends on the relative importance of flux and AO contrast, which will vary from tissue-to-tissue as optical properties vary. For instance, in this study, 576 nm still has a fairly high ΔAO and the flux is reasonable, but that may not be the case for tissues with higher concentrations of blood. Furthermore, the maximum permissible exposure (MPE) at each wavelength should be taken into account. For example, even though the detected flux is much lower at 1064 nm than at 576 nm, the MPE is five times higher. Practically, the choice of wavelength also depends on technological restrictions, such as the operating wavelength of a PRC. In what follows, we employ 1064 nm because it is the operating wavelength of the GaAs crystal previously employed for AO-guided HIFU,[24] it exhibits a good balance between detectable radiant flux and AO contrast, and the MPE is high.

Table 4 The properties of the PRC-based detection system. The values were chosen to match the setup employed in Ref. 24.

Property	Value
η_{det}	0.0040
A_d (cm^2)	0.2
α_c (cm^{-1})	1.8
L_c (cm)	0.7
γ' (cm^{-1})	0.5
γ'' (cm^{-1})	0

Table 5 The source/detector pair used for each geometry is used in Fig. 4(b). The source and detector locations are depicted in Fig. 4(a).

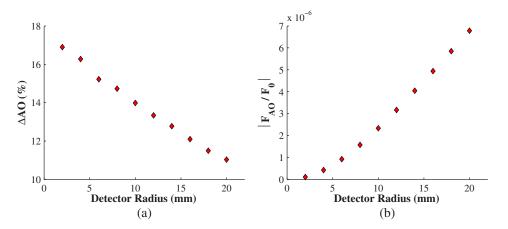| Source	R	T	Side
S_1	D_1	D_3	D_5
S_2	D_2	D_4	D_5
S_3	D_3	D_1	D_5

Fig. 5 (a) The AO signal contrast and (b) the detected AO radiant flux normalized by the illumination power of a ~30 mm³ HIFU lesion as a function of the detection aperture radius. The simulation geometry and properties are described in Sec. 3.1. AO radiant flux was calculated as the product of I_{AO} and A_d.

Table 6 The AO signal contrast and the detected AO radiant flux normalized by the illumination power of the ~30 mm³ lesion as a function of illumination wavelength. The optical wavelengths were chosen based on their biological or technical relevance. The optical properties of the bulk tissue and the lesion were based on Ref. 41.

λ (nm)	500	550	576	660	800	940	975	1064
$\Delta AO(\%)$	25.7	22.6	16.8	9.6	8.18	9.99	16.3	10.9
$\frac{|F_{AO}|}{S_0} \times 10^{-6}$	0.15	0.70	7.77	13.5	9.89	7.99	3.89	6.77

3.3 Robustness of the Acousto-Optic Signal

The goal of an AO-guided HIFU system is to use ΔAO as a feedback signal to control the volume of a lesion. In an ideal situation, the feedback signal would depend only on the volume of a lesion, and not other factors, such as the location of the lesion, the optical contrast, the thickness of the tissue, or the HIFU pressure amplitude used to create it. In reality, the AO signal will be affected by all of these parameters and in this section, we will seek to determine the robustness of the ΔAO to changes in tissue thickness, lesion optical contrast, and lesion position.

First, we compare the predicted ΔAO to that reported from experimental data,[24] where it was shown that for the case of a lesion in the center of chicken breast tissues of 15 to 30 mm thicknesses, the AO signal contrast of a lesion with a given volume is approximately independent of the tissue thickness and HIFU pressure amplitude. Here, the experimental apparatus is mimicked for tissues of thicknesses 20 to 30 mm and Fig. 6 shows ΔAO as a function of lesion volume, where thickness is in the x dimension, and it is equal to the source–detector separation distance.

It can be seen that ΔAO increases with lesion volume, but that the magnitude of the change is reduced as tissue thickness increases. The predictions bracket the experimental data for volumes less than 150 mm³ and suggest that the model captures the physical processes over this range. For larger volumes, the simulations predict the response to saturate and suggest less sensitivity to lesion volume, whereas the experimental data continue to increase. Reasons for these differences will be described in the discussion.

The effect of variations in the optical contrast of the lesion was considered based on data we have previously reported on *ex vivo* chicken breast.[41] Measurements of μ_s' as a function of thermal dose suggest a standard deviation of about 20%. In order to quantify the effect of lesion variabilities on the AO signal, the optical contrast of the lesion, C, is defined as follows:

$$C = \frac{(\Delta\mu)_{max}}{\mu_0}, \tag{12}$$
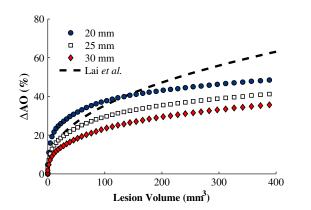

Fig. 6 The AO signal contrast as a function of lesion volume for tissues of 20 (blue circle), 25 (white box), and 30 (red diamond) mm thicknesses. The dashed black line is a best-fit derived from experimental data.[24] The simulation geometry and properties are described in Sec. 3.1. The lesions were computed using a 5.6-MPa peak focal pressure amplitude for the acoustic and thermal simulations, but the peak pressure was reduced to 100 kPa for the AO simulations.
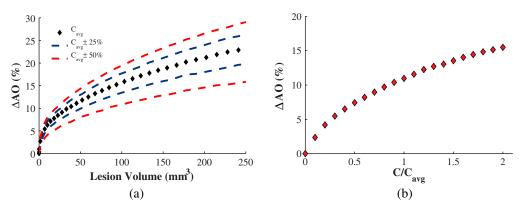
Fig. 7 (a) AO signal contrast as a function of lesion volume for lesions with C_{avg} (black diamonds), $C_{avg} \pm 25\%$ (blue line), and $C_{avg} \pm 50\%$ (red line). (b) AO signal contrast of the ~ 30 mm^3 lesion in the center of the volume as a function of its normalized optical contrast, C/C_{avg}. The simulation geometry and properties are described in Sec. 3.1.

where $(\Delta \mu)_{max}$ and μ_0 are defined in Eq. (5). Figure 7(a) shows ΔAO as a function of lesion volume for lesions with the average measured contrast at 1064 nm, C_{avg}, (black diamonds), $C_{avg} \pm 25\%$ (blue line), and $C_{avg} \pm 50\%$ (red line), which covers 2.5 standard deviations.

The average measured contrast is derived from the data presented in Table 3. Figure 7(b) shows ΔAO as a function of the normalized optical contrast of a single ~ 30 mm^3 lesion. For a 20% variation in contrast, ΔAO varies by about 1.3%.

The final lesion parameter affecting the AO signal investigated was the location of the lesion relative to the source and the detector. If ΔAO is not independent of location, a position-based adjustment must be applied to the prediction of lesion volume during HIFU. Figure 8 shows the impact of moving the lesion in all three directions, the x (optical source), y (lateral), and z (HIFU source), on ΔAO.

As the lesion is moved, the acoustic field moves with it so that the acoustic focus is always co-registered with the lesion. As the lesion is moved close to the optical source (along x), the AO detection sensitivity (indicated by the magnitude of ΔAO) increases proportionally with the amount of light that reaches

the acoustic focus, and it changes as the pressure field within the tissue is varied. As the lesion moves away from the center of the volume in y and z, the AO detection sensitivity decreases with the fluence of the light that reaches the acoustic focus. The physical mechanisms that cause the changes in the AO detection sensitivity are discussed further below. Overall, the results here demonstrate that ΔAO is not independent of lesion location and this is something that must be considered during HIFU guidance.

3.4 Treatment Strategy for Large Volumes

An important characteristic of a HIFU guidance technology is its ability to guide the treatment when forming an array of lesions as this is necessary to ablate large volumes. This was investigated by using ΔAO as a feedback signal to create an approximately cubic array of nine lesions. The tissue was exposed to HIFU until ΔAO reached 10%, which should result in a lesion of about 30 mm^3. The HIFU was then turned off, the tissue was allowed to cool for 30 s, and the HIFU transducer was moved to the next position. Although the thermal simulations were performed with 100-ms time steps, the AO feedback was calculated only every 5 s. This time was sufficiently small to capture the time dependence of the AO feedback, while maintaining a reasonable computational time. Figure 9 shows the resulting treatment volume after creating the lesion arrays starting (a) distal and (b) proximal to the light source, which is positioned at $(x, y, z) = (0, 20, 20)$ mm and projects downward from the "top" of the lesion array. The isosurfaces correspond to the volume, where the optical properties of the lesion reached $(\Delta \mu)_{max}$. In Fig. 9(a), the lesions were created by starting in the lower right and scanning in $-y$ and $-x$, respectively. This resulted in a uniform array of lesions, as would be desired. In Fig. 9(b), the array was created by starting in the upper right and scanning in $-y$ and $+x$, respectively, and it can be seen that each row of lesions is different and a uniform region of tissue has not been ablated. In this case, the presence of prior lesions resulted in a drop in the magnitude of ΔAO so that a longer insonation time was required to achieve the 10% change.

4 Discussion

In this work, we have investigated the design of an AO system for guiding HIFU treatments, assessed the robustness of its
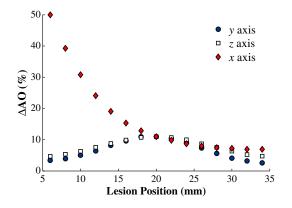

Fig. 8 AO signal contrast of the ~ 30 mm^3 lesion as its position within the volume was changed. The described lesion position is the location of the center of the lesion as it was scanned along the x (red diamonds), y (blue circles), and z (white squares) axes. The x axis was the optical source axis and the z axis was the HIFU propagation axis. The simulation geometry and properties are described in Sec. 3.1.
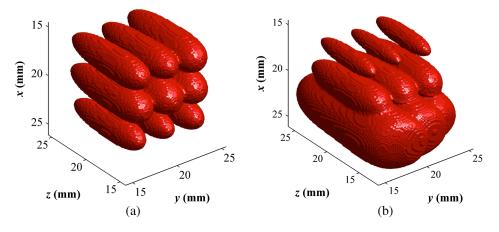
Fig. 9 Lesions arrays created using $\Delta AO = 10\%$ as a feedback condition to stop heating. Considering illumination from the "top," the arrays were created beginning (a) distal and (b) proximal to the illumination source. The simulation geometry and properties are described in Sec. 3. A time step of 100 ms was used for the thermal simulations, but the AO simulations were only performed at 5-s interval.

signal by considering changes in tissue thickness, lesion contrast, and lesion location, and evaluated the propriety of the technique for guiding the formation of lesion arrays to ablate large volumes. Overall, it was determined that for an optimal design, an AO-guided HIFU system should illuminate the target organ at 90 deg relative to the HIFU propagation using an optical wavelength, which exhibits low absorption in the tissue of interest, and detection should be performed in transmission using a large aperture detector. This arrangement, which is given by the S_2 source and D_4 detector in Fig. 4(a), has been determined to possess the optimum level of AO contrast, and it has been demonstrated to be suitable for guiding the ablation of large volumes.

As indicated in Sec. 2.3, the fluence of the modulated light is a function of the total light fluence and the magnitude of the ultrasound-induced phase modulation, which is dependent on the acoustic pressure. Therefore, where there is high fluence and high pressure, a significant amount of light is modulated. Although the highest acoustic pressures are present in the focus of the HIFU beam, Fig. 1 shows that there are also nonnegligible pressures present outside of the acoustic focus, particularly in the prefocal region of the acoustic field (near to D_1 in Fig. 4) and to a lesser extent in the postfocal region (near to D_3). Because the lesion is always located inside the focus of the acoustic field, ΔAO is always dependent on the amount of modulated light that is generated in the acoustic focus. However, it is also a function of the amount of detected light that was modulated outside the acoustic focus, which can sometimes be the dominant term. Ultimately, ΔAO will be highest when the light that is modulated inside the HIFU focus is maximized, and the light modulated outside the focus is minimized. The S_2 source and D_4 detector achieves this for two reasons. First, by having the light source normal to the HIFU propagation, the light does not have to travel through the entire prefocal region of the transducer in order to reach the focus. Therefore, the phase modulations that the light accumulates before reaching the focus are small. Second, because detection is in transmission mode, all of the light that is modulated before reaching the HIFU focus that reflects back out of the tissue never reaches the detector on the opposite side.

The optimal configuration for performing AO-guided HIFU requires access to three sides of the target organ. This is feasible for breast but may be impractical for most other organs. If

there is access to only two sides of an organ, then the best AO contrast is observed while illuminating opposite to the HIFU and detecting in transmission, as shown by S_3 and D_4. However, this geometry demonstrates only a marginally higher AO contrast than the configuration requiring access to only one side of the organ, which possesses significant practical advantages over a two-sided geometry.

With regard to the illumination wavelength, it was determined that the optimal wavelength is dependent upon the relative important of radiant flux (i.e., signal level) and AO contrast. Table 6 shows that when signal contrast is highest, signal level is generally lowest. For the purposes of AO-guided HIFU, where lesions are commonly formed deep within the body, the wavelength should normally be chosen to optimize signal level. Therefore, it is generally advisable to select a wavelength at which absorption and scattering are minimized, which will vary from tissue-to-tissue. Furthermore, it is also important to consider the wavelength-dependent MPE. Nevertheless, in practice, the optical wavelength is often dictated by technical restrictions. For example, the use of a GaAs PRC for detection requires the use of a 1064-nm source. Therefore, although Table 6 shows that using a 1064-nm source does not yield the highest signal level, it was still used for all of the simulations presented in this study.

Although it was demonstrated that an optimally designed AO-guidance system is able to successfully guide the formation of an array of HIFU lesions, it was determined that an appropriate treatment strategy must be employed. This is because the position of a lesion and the presence of pre-existing neighboring lesions impact the magnitude of ΔAO with respect to lesion volume. As Fig. 9(a) shows, the appropriate treatment strategy for creating an array of lesions is to begin distal to the optical source and then to move toward it after all distal lesions have been created. When lesions are first created proximal to the source, the fluence in the focus is higher and ΔAO is more sensitive to lesion volume. Thus, a smaller lesion is required to produce the same signal change close to the source than elsewhere in the volume. Additionally, when forming new lesions distal to the source, the pre-existing lesions cause a shadowing effect and less light reaches the HIFU focus than otherwise would. Thus, the change in the AO signal is less sensitive to lesion volume. Therefore, as the HIFU is moved away from the optical source, the lesions become larger. By starting treatment distal from the

optical source, there is no shadowing effect when creating the first row of lesions, and as the HIFU is moved closer to the source, the pre-existing lesions cause less modulated light to reach the detector, but this is offset by the increased sensitivity of the AO signal with respect to lesion volume.

While employing the aforementioned strategy to guide the formation of lesion arrays should be effective in a homogenous medium, the results in Fig. 9 suggest that AO guidance is sensitive to the optical properties of the surrounding tissue. Not only could the feedback signal be affected by pre-existing lesions, but it could also be affected by nearby optical inhomogeneities in the tissue, which are almost certain to be present *in vivo*. Therefore, in practice, it may be necessary to image the area surrounding the treatment volume prior to ablating. Quantitative AO imaging[49,50] has recently been proposed as a method for quantifying the optical properties of tissue *in situ* and could potentially be used prior to AO-guided HIFU surgeries in order to predict the response of ΔAO to lesion volume. Another option for quantifying optical properties prior to ablation could be pressure contrast imaging.[51]

This study has also demonstrated that the AO signal is affected by changes in tissue thickness, lesion optical contrast, and lesion position. By adjusting the thickness of the tissue and the position of the lesion, it has been shown that the sensitivity of the AO signal with respect to lesion volume scales with the local fluence of the light in the HIFU focus. Nevertheless, if the optical properties of the target organ are imaged before HIFU treatments, a forward model can be applied to adjust predictions of lesion volumes based on ΔAO. However, even with *a priori* knowledge of the target organ's optical properties, there will still be variability in the optical properties of the lesions. Therefore, the sensitivity of the AO signal to changes in lesion contrast is important to characterize in order to quantify the uncertainty in lesion volume predictions. As Fig. 7(b) demonstrates, a doubling of the optical contrast of a $\sim$30 mm^3 lesion results in a shift of ΔAO by $<$5%. While this seems like a small shift in response, Fig. 7(a) demonstrates that for a 30 mm^3 lesion with average optical properties, a 25% uncertainty results in a prediction of a lesion volume between $\sim$20 and 45 mm^3 and a 50% uncertainty results in a prediction of a lesion volume between $\sim$8 and 75 mm^3. As the lesion volume increases, the uncertainties become even greater. For example, a 25% uncertainty in the optical properties of a 100 mm^3 lesion results in a volume prediction between $\sim$75 and 145 mm^3, and a 50% uncertainty results in a prediction between $\sim$65 and 250 mm^3. Thus, if a high level of accuracy is required for predictions of lesion volume, it may be advisable to use only AO guidance for lesion volumes on the order of the HIFU focus or smaller.

While examining the robustness of the AO signal to changes in tissue thickness, it was determined that simulations underpredict ΔAO for large lesion volumes compared to experimental data. As the lesion grows outside the HIFU focus, the simulation predicts that ΔAO starts to saturate, while the experimental data continue to increase with respect to lesion volume. The most glaring difference between the AO model and the experimental parameters used in Ref. 24 is the pressure amplitude. As previously discussed, the assumptions used to calculate phase modulations limit the peak pressure of the model to 100 kPa, while a variety of peak pressures, up to 10 MPa, were used in the experiments from which the data in Fig. 6 were derived. In the model, the pressures outside the HIFU focus are too low to significantly contribute to each photon packet's total phase shift (except for in

some pre- and postfocal locations). Alternatively, during experiments, the pressure amplitudes outside the focus may still be quite high and could in fact contribute significantly to the total phase shift of each optical path. This would result in the AO signal being more sensitive to optical changes outside the HIFU focus, thus inducing a larger ΔAO for larger lesion volumes.

There were other physical effects that the numerical model did not capture, including acoustic nonlinearity. For the high experimental pressure amplitudes *in situ*, we would anticipate nonlinear distortion effects to result in spatial and temporal changes to the acoustic field, although these should be modest for the fundamental acoustic frequency, which is typically what is detected in AO systems. Additionally, the acoustic attenuation of tissue is temperature dependent. This temperature dependence will result in a spatial distribution of acoustic attenuation, which will reflect the thermal field. The angular spectrum code employed here cannot capture inhomogeneities of this sort. We recommend that models consider these effects in the future to determine if they result in significant changes to the AO signals.

5 Conclusions

In this study, a numerical model was developed to determine an optimal design for an AO-guided HIFU system. The angular spectrum method was used to model the acoustic field from the HIFU source. The temperature field, due to the absorption of ultrasound, was modeled using a finite-difference time-domain solution to the Pennes bioheat equation. Changes in tissue optical properties were calculated using a thermal dose model derived from measurements of optical property changes. Light propagation was modeled using an open-source GPU-accelerated MC algorithm, modified to account for light-sound interactions and to account for AO signal detection. Using the model, it was shown that it is optimal to illuminate the tissue with an optical wavelength exhibiting low absorption in tissue at 90 deg relative to the HIFU propagation and to detect light in transmission with a large aperture detector. The effects of tissue thickness, lesion optical contrast, lesion position, and the presence or absence of neighboring lesions on the AO signal were evaluated. Using information gathered during this study, it was shown that the optimal strategy for treating large tissue volumes is to create a lesion array beginning distal to the source and moving toward it.

References

1. K. Hynynen et al., "A clinical, noninvasive, MR imaging-monitored ultrasound surgery method," *Radiographics* **16**(1), 185–195 (1996).

2. J. E. Kennedy, "High-intensity focused ultrasound in the treatment of solid tumours," *Nat. Rev. Cancer* **5**(4), 321–327 (2005).

3. E. A. Stewart et al., "Focused ultrasound treatment of uterine fibroid tumors: safety and feasibility of a noninvasive thermoablative technique," *Am. J. Obstet. Gynecol.* **189**(1), 48–54 (2003).

4. W. J. Elias et al., "A pilot study of focused ultrasound thalamotomy for essential tremor," *N. Engl. J. Med.* **369**(7), 640–648 (2013).

5. T. J. Dubinsky et al., "High-intensity focused ultrasound: current potential and oncologic applications," *Am. J. Roentgenol.* **190**(1), 191–199 (2008).

6. I. Rivens et al., "Treatment monitoring and thermometry for therapeutic focused ultrasound," *Int. J. Hyperthermia* **23**(2), 121–139 (2007).

7. G. ter Haar, D. Sinnett, and I. Rivens, "High intensity focused ultrasound-a surgical technique for the treatment of discrete liver tumours," *Phys. Med. Biol.* **34**(11), 1743–1750 (1989).

8. N. T. Sanghvi et al., "Noninvasive surgery of prostate tissue by high-intensity focused ultrasound," *IEEE Trans. Ultrason. Ferroelectr. Freq. Control* **43**(6), 1099–1110 (1996).

9. F. Wu et al., "Extracorporeal focused ultrasound surgery for treatment of human solid carcinomas: early Chinese clinical experience," *Ultrasound Med. Biol.* **30**(2), 245–260 (2004).

10. N. McDannold, "Quantitative MRI-based temperature mapping based on the proton resonant frequency shift: review of validation studies," *Int. J. Hyperthermia* **21**(6), 533–546 (2005).

11. C. Hill and G. Ter Haar, "High intensity focused ultrasound—potential for cancer treatment," *Br. J. Radiol.* **68**(816), 1296–1303 (1995).

12. S. Vaezy et al., "Real-time visualization of high-intensity focused ultrasound treatment using ultrasound imaging," *Ultrasound Med. Biol.* **27**(1), 33–42 (2001).

13. B. A. Rabkin, V. Zderic, and S. Vaezy, "Hyperecho in ultrasound images of HIFU therapy: involvement of cavitation," *Ultrasound Med. Biol.* **31**(7), 947–956 (2005).

14. B. A. Rabkin et al., "Biological and physical mechanisms of HIFU-induced hyperecho in ultrasound images," *Ultrasound Med. Biol.* **32**(11), 1721–1729 (2006).

15. C. C. Coussios et al., "Role of acoustic cavitation in the delivery and monitoring of cancer treatment by high-intensity focused ultrasound (HIFU)," *Int. J. Hyperthermia* **23**(2), 105–120 (2007).

16. P. M. Meaney, M. D. Cahill, and G. ter Haar, "The intensity dependence of lesion position shift during focused ultrasound surgery," *Ultrasound Med. Biol.* **26**(3), 441–450 (2000).

17. M. R. Bailey et al., "Use of overpressure to assess the role of bubbles in focused ultrasound lesion shape *in vitro*," *Ultrasound Med. Biol.* **27**(5), 695–708 (2001).

18. T. D. Khokhlova et al., "Magnetic resonance imaging of boiling induced by high intensity focused ultrasound," *J. Acoust. Soc. Am.* **125**(4), 2420–2431 (2009).

19. S. A. Sapareto and W. C. Dewey, "Thermal dose determination in cancer therapy," *Int. J. Radiat. Oncol. Biol. Phys.* **10**(6), 787–800 (1984).

20. C. M. Tempany et al., "Focused ultrasound surgery in oncology: overview and principles," *Radiology* **259**(1), 39–56 (2011).

21. T. Robinson and P. Lele, "An analysis of lesion development in the brain and in plastics by high-intensity focused ultrasound at low-megahertz frequencies," *J. Acoust. Soc. Am.* **51**(4B), 1333–1351 (1972).

22. R. Righetti et al., "Elastographic characterization of HIFU-induced lesions in canine livers," *Ultrasound Med. Biol.* **25**(7), 1099–1113 (1999).

23. A. R. Funke et al., "Photoacoustic guidance of high intensity focused ultrasound with selective optical contrasts and time-reversal," *Appl. Phys. Lett.* **94**(5), 054102 (2009).

24. P. Lai et al., "Real-time monitoring of high-intensity focused ultrasound lesion formation using acousto-optic sensing," *Ultrasound Med. Biol.* **37**(2), 239–252 (2011).

25. T. W. Murray, P. Lai, and R. A. Roy, "Measuring tissue properties and monitoring therapeutic responses using acousto-optic imaging," *Annal. Biomed. Eng.* **40**(2), 474–485 (2012).

26. S. Thomsen and J. A. Pearce, Chapter 13, *Optical-Thermal Response of Laser-Irradiated Tissue*, 2nd ed., pp. 487–549, Springer Science +Business Media, Berlin (2011).

27. J. F. Black and J. K. Barton, "Chemical and structural changes in blood undergoing laser photocoagulation," *Photochem. Photobiol.* **80**(1), 89–97 (2004).

28. W. Leutz and G. Maret, "Ultrasonic modulation of multiply scattered light," *Phys. B* **204**(1), 14–19 (1995).

29. L. V. Wang, "Mechanisms of ultrasonic modulation of multiply scattered coherent light: an analytic model," *Phys. Rev. Lett.* **87**(4), 043903 (2001).

30. S. Sakadžić and L. V. Wang, "Ultrasonic modulation of multiply scattered coherent light: an analytical model for anisotropically scattering media," *Phys. Rev. E* **66**(2), 026603 (2002).

31. S. Sakadžić and L. V. Wang, "Modulation of multiply scattered coherent light by ultrasonic pulses: an analytical model," *Phys. Rev. E* **72**(3), 036620 (2005).

32. P. R. Stepanishen and K. C. Benjamin, "Forward and backward projection of acoustic fields using FFT methods," *J. Acoust. Soc. Am.* **71**(4), 803–812 (1982).

33. J. W. Goodman, *Introduction to Fourier Optics*, Roberts and Company Publishers, Greenwood Village, Colorado (2005).

34. P. Wu and T. Stepinski, "Extension of the angular spectrum approach to curved radiators," *J. Acoust. Soc. Am.* **105**(5), 2618–2627 (1999).

35. J. Jiménez and E. Hita, "Babinet's principle in scalar theory of diffraction," *Opt. Rev.* **8**(6), 495–497 (2001).

36. H. O'Neil, "Theory of focusing radiators," *J. Acoust. Soc. Am.* **21**(5), 516–526 (1949).

37. H. H. Pennes, "Analysis of tissue and arterial blood temperatures in the resting human forearm," *J. Appl. Physiol.* **1**(2), 93–122 (1948).

38. W. Ames, Chapter 5, *Numerical Methods for Partial Differential Equations*, Academic Press, San Diego (1992).

39. K. J. Parker, "The thermal pulse decay technique for measuring ultrasonic absorption coefficients," *J. Acoust. Soc. Am.* **74**(5), 1356–1361 (1983).

40. K. J. Parker, "Effects of heat conduction and sample size on ultrasonic absorption measurements," *J. Acoust. Soc. Am.* **77**(2), 719–725 (1985).

41. M. T. Adams et al., "Thermal dose dependent optical property changes of ex vivo chicken breast tissues between 500 and 1100 nm," *Phys. Med. Biol.* **59**(13), 3249–3260 (2014).

42. L. Huang and L.-S. Liu, "Simultaneous determination of thermal conductivity and thermal diffusivity of food and agricultural materials using a transient plane-source method," *J. Food Eng.* **95**(1), 179–185 (2009).

43. R. Y. Rubinstein and D. P. Kroese, *Simulation and the Monte Carlo Method*, Vol. **707**, John Wiley & Sons, Hoboken, New Jersey (2011).

44. Q. Fang and D. A. Boas, "Monte Carlo simulation of photon migration in 3D turbid media accelerated by graphics processing units," *Opt. Express* **17**(22), 20178–20190 (2009).

45. S. Sakadžić and L. V. Wang, "Correlation transfer equation for ultrasound-modulated multiply scattered light," *Phys. Rev. E* **74**(3), 036618 (2006b).

46. T. W. Murray et al., "Detection of ultrasound-modulated photons in diffuse media using the photorefractive effect," *Opt. Lett.* **29**(21), 2509–2511 (2004).

47. S. Sakadžić and L. V. Wang, "Correlation transfer and diffusion of ultrasound-modulated multiply scattered light," *Phys. Rev. Lett.* **96**, 163902 (2006).

48. S. Powell and T. S. Leung, "Highly parallel Monte-Carlo simulations of the acousto-optic effect in heterogeneous turbid media," *J. Biomed. Opt.* **17**(4), 045002 (2012).

49. S. Powell and T. S. Leung, "Linear reconstruction of absorption perturbations in coherent ultrasound-modulated optical tomography," *J. Biomed. Opt.* **18**(12), 126020 (2013).

50. S. Powell and T. S. Leung, "Quantitative reconstruction of absorption and scattering coefficients in ultrasound-modulated optical tomography," *Proc. SPIE* **8943**, 89434X (2014).

51. P. Lai, R. A. Roy, and T. W. Murray, "Quantitative characterization of turbid media using pressure contrast acousto-optic imaging," *Opt. Lett.* **34**(18), 2850–2852 (2009).

Matthew T. Adams is a research and advanced development engineer at Bose Corporation. He received his doctoral degree in mechanical engineering from Boston University, during which he was a Whitaker Fellow in the Institute of Biomedical Engineering at the University of Oxford, United Kingdom. His research interests focus on the application of wave physics to solving complex biomedical, underwater, and hearing-related problems.

Robin O. Cleveland is a professor of engineering science at the University of Oxford. Previously he spent fourteen years at Boston University, rising to rank of professor of mechanical engineering. His research includes shock wave lithotripsy, high intensity focused ultrasound, and drug delivery. He is a fellow of the Acoustical Society of America and a past associate editor of that society's journal and past board member of the International Society of Therapeutic Ultrasound.

Ronald A. Roy is a professor of mechanical engineering at the University of Oxford, United Kingdom. He specializes in the application of physical acoustics principles to problems in biomedical acoustics, industrial ultrasonics, and acoustical oceanography, with a focus on acoustic cavitation and the acoustics of bubbly media. He is a fellow of the Acoustical Society of America and a recipient of the ASA Helmholtz-Rayleigh Interdisciplinary Silver Medal.